High-acceptance versatile microfocus module based on elliptical Fresnel zone plates for small-angle X-ray scattering

MAXIME LEBUGLE,[1,*] MARIANNE LIEBI,[1,2] KLAUS WAKONIG,[1] VITALIY A. GUZENKO,[1] MIRKO HOLLER,[1] ANDREAS MENZEL,[1] MANUEL GUIZAR-SICAIROS,[1] ANA DIAZ,[1] AND CHRISTIAN DAVID[1]

[1]Paul Scherrer Institut, CH 5232 Villigen-PSI, Switzerland
[2]Current address: MAX IV Laboratory, Lund University, 221-00 Lund, Sweden
*maxime.lebugle@psi.ch

Abstract: High-efficiency microfocusing of multi-keV X-rays at synchrotron sources is highly profitable for spatially resolved structural analysis of many kinds. Because radiation from synchrotron sources is typically elongated along the horizontal dimension, generating a microbeam that is isotropic in size requires a carefully designed optics system. Here we report on using a combination of a horizontally tunable slit downstream of the undulator source with elliptical diffractive Fresnel zone plates. We demonstrate the arrangement in context of small-angle X-ray scattering experiments, obtaining a microbeam of 2.2 μm × 1.8 μm (X × Y) with a flux of 1.2×10^{10} photons/s at an energy of 11.2 keV at the sample position.

References and links

1. C. Riekel, M. Burghammer, and G. Schertler, "Protein crystallography microdiffraction," Curr. Opin. Struct. Biol. **15**(5), 556–562 (2005).
2. J. L. Smith, R. F. Fischetti, and M. Yamamoto, "Micro-crystallography comes of age," Curr. Opin. Struct. Biol. **22**(5), 602–612 (2012).
3. A. Alatas, B. M. Leu, J. Zhao, H. Yavas, T. S. Toellner, and E. E. Alp, "Improved focusing capability for inelastic X-ray spectrometer at 3-ID of the APS: A combination of toroidal and Kirkpatrick-Baez (KB) mirrors," Nuclear Instruments & Methods in Physics Research Section a-Accelerators Spectrometers Detectors and Associated Equipment **649**(1), 166–168 (2011).
4. T. Warwick, K. Frank, J. B. Kortright, G. Meigs, M. Moronne, S. Myneni, E. Rotenberg, S. Seal, and W. F. Steele, "A scanning transmission x-ray microscope for materials science spectromicroscopy at the advanced light source," Rev. Sci. Instrum. **69**(8), 2964–2973 (1998).
5. J. Stangl, C. Mocuta, A. Diaz, T. H. Metzger, and G. Bauer, "X-ray diffraction as a local probe tool," ChemPhysChem **10**(17), 2923–2930 (2009).
6. T. Etzelstorfer, M. J. Süess, G. L. Schiefler, V. L. R. Jacques, D. Carbone, D. Chrastina, G. Isella, R. Spolenak, J. Stangl, H. Sigg, and A. Diaz, "Scanning X-ray strain microscopy of inhomogeneously strained Ge micro-bridges," J. Synchrotron Radiat. **21**(Pt 1), 111–118 (2014).
7. M. D. de Jonge and S. Vogt, "Hard X-ray fluorescence tomography - an emerging tool for structural visualization," Curr. Opin. Struct. Biol. **20**(5), 606–614 (2010).
8. P. Fratzl, "Small-angle scattering in materials science-a short review of applications in alloys, ceramics and composite materials," J. Appl. Cryst. **36**(3), 397–404 (2003).
9. P. Fratzl, H. F. Jakob, S. Rinnerthaler, P. Roschger, and K. Klaushofer, "Position-resolved small-angle x-ray scattering of complex biological materials," J. Appl. Cryst. **30**(5), 765–769 (1997).
10. C. Giannini, D. Siliqi, M. Ladisa, D. Altamura, A. Diaz, A. Beraudi, T. Sibillano, L. De Caro, S. Stea, F. Baruffaldi, and O. Bunk, "Scanning SAXS–WAXS microscopy on osteoarthritis-affected bone–an age-related study," J. Appl. Cryst. **47**(1), 110–117 (2014).
11. C. Y. J. Hémonnot, J. Reinhardt, O. Saldanha, J. Patommel, R. Graceffa, B. Weinhausen, M. Burghammer, C. G. Schroer, and S. Köster, "X-rays reveal the internal structure of keratin bundles in whole cells," ACS Nano **10**(3), 3553–3561 (2016).
12. M. Bernhardt, J. D. Nicolas, M. Eckermann, B. Eltzner, F. Rehfeldt, and T. Salditt, "Anisotropic x-ray scattering and orientation fields in cardiac tissue cells," New J. Phys. **19**(1), 013012 (2017).
13. K. Jefimovs, J. Vila-Comamala, T. Pilvi, J. Raabe, M. Ritala, and C. David, "Zone-doubling technique to produce ultrahigh-resolution x-ray optics," Phys. Rev. Lett. **99**(26), 264801 (2007).
14. S. Gorelick, J. Vila-Comamala, V. A. Guzenko, R. Barrett, M. Salomé, and C. David, "High-efficiency Fresnel zone plates for hard X-rays by 100 keV e-beam lithography and electroplating," J. Synchrotron Radiat. **18**(Pt 3), 442–446 (2011).

15. I. Mohacsi, P. Karvinen, I. Vartiainen, V. A. Guzenko, A. Somogyi, C. M. Kewish, P. Mercere, and C. David, "High-efficiency zone-plate optics for multi-keV X-ray focusing," J. Synchrotron Radiat. **21**(3), 497–501 (2014).

16. C. G. Schroer, O. Kurapova, J. Patommel, P. Boye, J. Feldkamp, B. Lengeler, M. Burghammer, C. Riekel, L. Vincze, A. van der Hart, and M. Küchler, "Hard X-ray nanoprobe based on refractive x-ray lenses," Appl. Phys. Lett. **87**(12), 124103 (2005).

17. G. B. M. Vaughan, J. P. Wright, A. Bytchkov, M. Rossat, H. Gleyzolle, I. Snigireva, and A. Snigirev, "X-ray transfocators: focusing devices based on compound refractive lenses," J. Synchrotron Radiat. **18**(Pt 2), 125–133 (2011).

18. O. Hignette, P. Cloetens, G. Rostaing, P. Bernard, and C. Morawe, "Efficient sub 100 nm focusing of hard x rays," Rev. Sci. Instrum. **76**(6), 1–5 (2005).

19. J. Vila-Comamala, A. Diaz, M. Guizar-Sicairos, A. Mantion, C. M. Kewish, A. Menzel, O. Bunk, and C. David, "Characterization of high-resolution diffractive X-ray optics by ptychographic coherent diffractive imaging," Opt. Express **19**(22), 21333–21344 (2011).

20. C. G. Schroer, P. Boye, J. M. Feldkamp, J. Patommel, A. Schropp, A. Schwab, S. Stephan, M. Burghammer, S. Schöder, and C. Riekel, "Coherent x-ray diffraction imaging with nanofocused illumination," Phys. Rev. Lett. **101**(9), 090801 (2008).

21. B. Nöhammer, C. David, M. Burghammer, and C. Riekel, "Coherence-matched micro focusing of hard x-rays," Appl. Phys. Lett. **86**(16), 163804 (2005).

22. H. Ade, C. H. Ko, and E. Anderson, "Astigmatism correction in x-ray scanning photoemission microscope with use of elliptical zone plate," Appl. Phys. Lett. **60**(9), 1040–1042 (1992).

23. V. A. Guzenko, J. Romijn, J. Vila-Comamala, S. Gorelick, and C. David, "Efficient E-Beam Lithography Exposure Strategies for Diffractive X-ray Optics," AIP Conf. Proc. **1365**, 92 (2012).

24. S. Gorelick, V. A. Guzenko, J. Vila-Comamala, and C. David, "Direct e-beam writing of dense and high aspect ratio nanostructures in thick layers of PMMA for electroplating," Nanotechnology **21**(29), 295303 (2010).

25. A. Diaz, C. Mocuta, J. Stangl, M. Keplinger, T. Weitkamp, F. Pfeiffer, C. David, T. H. Metzger, and G. Bauer, "Coherence and wavefront characterization of Si-111 monochromators using double-grating interferometry," J. Synchrotron Radiat. **17**(3), 299–307 (2010).

26. M. Holler, A. Diaz, M. Guizar-Sicairos, P. Karvinen, E. Färm, E. Härkönen, M. Ritala, A. Menzel, J. Raabe, and O. Bunk, "X-ray ptychographic computed tomography at 16 nm isotropic 3D resolution," Sci. Rep. **4**(1), 3857 (2015).

27. D. A. Shapiro, Y.-S. Yu, T. Tyliszczak, J. Cabana, R. Celestre, W. Chao, K. Kaznatcheev, A. L. D. Kilcoyne, F. Maia, S. Marchesini, Y. S. Meng, T. Warwick, L. L. Yang, and H. A. Padmore, "Chemical composition mapping with nanometre resolution by soft X-ray microscopy," Nat. Photonics **8**(10), 765–769 (2014).

28. J. Deng, D. J. Vine, S. Chen, Y. S. Nashed, Q. Jin, N. W. Phillips, T. Peterka, R. Ross, S. Vogt, and C. J. Jacobsen, "Simultaneous cryo X-ray ptychographic and fluorescence microscopy of green algae," Proc. Natl. Acad. Sci. U.S.A. **112**(8), 2314–2319 (2015).

29. M. Holler, M. Guizar-Sicairos, E. H. Tsai, R. Dinapoli, E. Müller, O. Bunk, J. Raabe, and G. Aeppli, "High-resolution non-destructive three-dimensional imaging of integrated circuits," Nature **543**(7645), 402–406 (2017).

30. M. Guizar-Sicairos and J. R. Fienup, "Measurement of coherent x-ray focused beams by phase retrieval with transverse translation diversity," Opt. Express **17**(4), 2670–2685 (2009).

31. A. Schropp, P. Boye, J. M. Feldkamp, R. Hoppe, J. Patommel, D. Samberg, S. Stephan, K. Giewekemeyer, R. N. Wilke, T. Salditt, J. Gulden, A. P. Mancuso, I. A. Vartanyants, E. Weckert, S. Schöder, M. Burghammer, and C. G. Schroer, "Hard X-ray nanobeam characterization by coherent diffraction microscopy," Appl. Phys. Lett. **96**(9), 091102 (2010).

32. M. Guizar-Sicairos, S. Narayanan, A. Stein, M. Metzler, A. R. Sandy, J. R. Fienup, and K. Evans-Lutterodt, "Measurement of hard X-ray lens wavefront aberrations using phase retrieval," Appl. Phys. Lett. **98**(11), 111108 (2011).

33. J. Vila-Comamala, A. Diaz, M. Guizar-Sicairos, A. Mantion, C. M. Kewish, A. Menzel, O. Bunk, and C. David, "Characterization of high-resolution diffractive X-ray optics by ptychographic coherent diffractive imaging," Opt. Express **19**(22), 21333–21344 (2011).

34. F. Seiboth, A. Schropp, M. Scholz, F. Wittwer, C. Rödel, M. Wünsche, T. Ullsperger, S. Nolte, J. Rahomäki, K. Parfeniukas, S. Giakoumidis, U. Vogt, U. Wagner, C. Rau, U. Boesenberg, J. Garrevoet, G. Falkenberg, E. C. Galtier, H. Ja Lee, B. Nagler, and C. G. Schroer, "Perfect X-ray focusing via fitting corrective glasses to aberrated optics," Nat. Commun. **8**, 14623 (2017).

35. X. Huang, H. Yan, R. Harder, Y. Hwu, I. K. Robinson, and Y. S. Chu, "Optimization of overlap uniformness for ptychography," Opt. Express **22**(10), 12634–12644 (2014).

36. M. Guizar-Sicairos, I. Johnson, A. Diaz, M. Holler, P. Karvinen, H.-C. Stadler, R. Dinapoli, O. Bunk, and A. Menzel, "High-throughput ptychography using Eiger: scanning X-ray nano-imaging of extended regions," Opt. Express **22**(12), 14859–14870 (2014).

37. P. Thibault and A. Menzel, "Reconstructing state mixtures from diffraction measurements," Nature **494**(7435), 68–71 (2013).

38. F. Zhang, J. Ilavsky, G. G. Long, J. P. Quintana, A. J. Allen, and P. R. Jemian, "Glassy carbon as an absolute intensity calibration standard for small-angle scattering," Metall. Trans., A, Phys. Metall. Mater. Sci. **41**(5), 1151–1158 (2010).

39. S. Rinnerthaler, P. Roschger, H. F. Jakob, A. Nader, K. Klaushofer, and P. Fratzl, "Scanning small angle X-ray scattering analysis of human bone sections," Calcif. Tissue Int. **64**(5), 422–429 (1999).

40. S. Pabisch, W. Wagermaier, T. Zander, C. Li, and P. Fratzl, "Imaging the Nanostructure of Bone and Dentin Through Small- and Wide-Angle X-ray Scattering," Methods Enzymol. **532**, 391–413 (2013).
41. M. Liebi, M. Georgiadis, A. Menzel, P. Schneider, J. Kohlbrecher, O. Bunk, and M. Guizar-Sicairos, "Nanostructure surveys of macroscopic specimens by small-angle scattering tensor tomography," Nature **527**(7578), 349–352 (2015).
42. M. Georgiadis, M. Guizar-Sicairos, O. Gschwend, P. Hangartner, O. Bunk, R. Müller, and P. Schneider, "Ultrastructure Organization of Human Trabeculae Assessed by 3D sSAXS and Relation to Bone Microarchitecture," PLoS One **11**(8), e0159838 (2016).
43. P. Kraft, A. Bergamaschi, Ch. Broennimann, R. Dinapoli, E. F. Eikenberry, B. Henrich, I. Johnson, A. Mozzanica, C. M. Schlepütz, P. R. Willmott, and B. Schmitt, "Performance of single-photon-counting PILATUS detector modules," J. Synchrotron Radiat. **16**(3), 368–375 (2009).
44. M. Georgiadis, M. Guizar-Sicairos, A. Zwahlen, A. J. Trüssel, O. Bunk, R. Müller, and P. Schneider, "3D scanning SAXS: a novel method for the assessment of bone ultrastructure orientation," Bone **71**, 42–52 (2015).
45. O. Bunk, M. Bech, T. H. Jensen, R. Feidenhans'l, T. Binderup, A. Menzel, and F. Pfeiffer, "Multimodal x-ray scatter imaging," New J. Phys. **11**(12), 123016 (2009).

1. Introduction

Focusing X-ray beams to a size of a few micrometers is often used in synchrotron beamlines when the flux density needs to be increased to probe volumes of correspondingly small size, *e.g.* in protein crystallography [1, 2] or in high-pressure *in situ* experiments with diamond anvil cells [3]. In scanning-probe experiments with a microfocused X-ray beam, different imaging modalities exist depending on the nature of the signal which is probed, *e.g.* the attenuation through a sample in scanning transmission X-ray microscopy [4], the diffraction signal of a crystal when one of its planes is in Bragg condition in scanning X-ray diffraction microscopy [5, 6], or the fluorescence signal produced when the X-ray energy is larger than the binding energy of the electrons in the atoms in scanning X-ray fluorescence microscopy [7]. Small-angle X-ray scattering (SAXS) is yet another signal that can be exploited in scanning-probe experiments, typically at wavelengths around 1 Å. SAXS patterns can be recorded with 2D pixelated detectors and contain information about the specimen structure on the nanometer length scale, averaged over the illuminated sample volume. Spatially resolved SAXS, or scanning SAXS, has proven to be a useful method, *e.g.* for the characterization of synthetic and biological materials [8, 9], medical studies [10] and cellular structure characterization [11, 12].

X-ray focusing can be achieved with many types of X-ray optics. Fresnel zone plates (FZPs) provide focal spots with sizes down to few tens of nanometers, albeit with rather limited efficiency [13]. More efficient devices for nanofocusing can be built at energies up to about 10 keV [14], for instance by using complex lithography techniques [15]. For higher X-ray energies, other focusing optics such as compound refractive lenses [16, 17] and Kirkpatrick-Baez (KB) mirrors [18] are commonly used.

In all scanning X-ray microscopy techniques, 2D images can be obtained. Each pixel contains local information about the sample, the type of which depends on the nature of the signal. In these images the pixel size is determined by the scanning step while the size of the focused beam limits the spatial resolution. It is often desirable to have a round focused beam, *i.e.* a beam with approximately equal size along both scanning directions. However, due to the elongation of the beam profile along the horizontal dimension in most synchrotron sources, geometrical demagnification of the source by a lens will result in a correspondingly elongated focused spot. Therefore, strategies to reduce the horizontal beam size and to achieve a round focus have been sought. Using a horizontally tunable slit near the focus plane one can cut down the focused beam to some extent, however this can cause parasitic scattering with detrimental consequences in certain scanning-probe experiments, in particular in scanning SAXS. A round diffraction-limited focused beam can be obtained using a FZP [19], however this approach requires transverse coherent illumination over the entire lens. Other X-ray optical schemes combine two crossed 1D lenses for the horizontal and vertical dimensions to achieve different demagnification factors and a diffraction-limited beam, using refractive [20] or diffractive [21] lenses, at the cost of a more complex alignment procedure. Diffraction-limited focusing is a good solution for achieving nanofocused beams, however for

micrometer spot sizes alternative solutions providing a round beam with high flux would be desirable.

Here, we report on a microfocus module, based on a horizontally tunable slit at 12.1 m downstream from the X-ray source to effectively reduce the horizontal source size together with the use of elliptical FZPs to account for the astigmatism originating from the different positions of the vertical and horizontal sources along the optical axis. We demonstrate that this approach produces a focused beam of the order of 1.8 μm in the vertical dimension and, depending on the slit opening, in the range of 2.2–12.1 μm in the horizontal one, with a flux varying from 1.2×10^{10} to 1.2×10^{11} photons/s at 11.2 keV. For an open slit a geometrical demagnification of the undulator source is done by using a conventional, circular FZP. In comparison with other focusing schemes producing round microfocus spots, our system is very efficient, as it does not require a coherent illumination. Furthermore, its alignment is extremely simple. We demonstrate the application of this focusing module in a scanning SAXS experiment on a thin slice of human trabecular bone, revealing the changes in the orientation of its collagen fibers with spatial resolution given by the microfocus size.

2. Microfocus module design

The experiments were carried out at the cSAXS beamline, Swiss Light Source at the Paul Scherrer Institut in Villigen, Switzerland. Figure 1(a) shows the designed optical layouts, in which X and Y denote the horizontal and vertical dimensions, respectively, and where the beam propagates along the optical axis, Z. The undulator delivers a source with a size of 200 μm × 20 μm (X × Y) at full-width half maximum (FWHM). A fixed-exit double-crystal Si(111) monochromator defines the X-ray energy with bandwidth of about 2×10^{-4}. All diffractive FZPs were mounted in an ultra-high vacuum chamber, placed 1.9 m upstream of the sample. The FZPs are used together with a central stop with diameter of 160 μm and an order-sorting square aperture with a width of 150 μm to select the first diffraction order only.
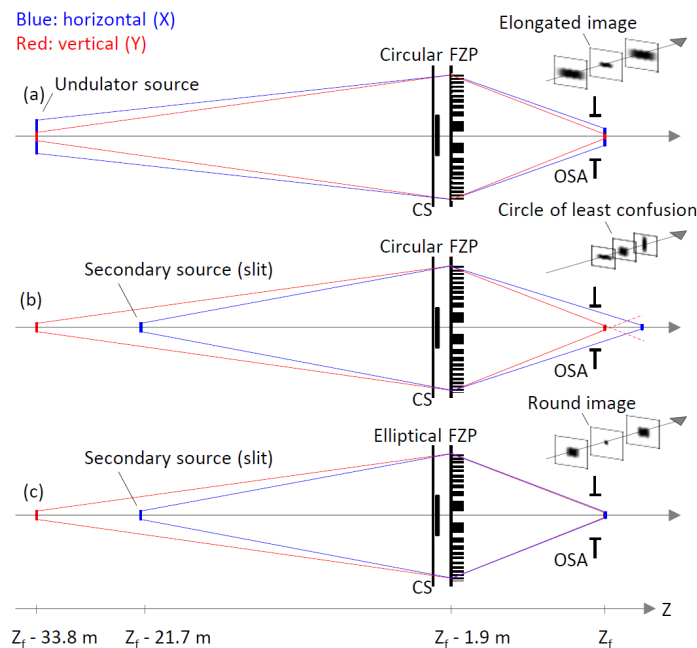

Fig. 1. Optical layouts. (a) Imaging with a circular FZP, which produces an elongated focus at $Z = Z_f$. (b) Imaging with a secondary source in X and a circular FZP. The beam presents on-axis astigmatism and the circle of least confusion reached at $Z > Z_f$ is most favorable for isotropic resolution. (c) Imaging with a specially designed elliptical FZP to cancel out the on-axis astigmatism and obtain a round focus at $Z = Z_f$. The sketches close to each focal plane schematize the different spot shapes along the Z axis.

When the slit is fully open, a demagnified image of the source can be formed at the sample location by using a circular FZP, Fig. 1(a). With our setup distances, a focal length of $f_0 = 1793$ mm is required, which leads to a demagnification factor of 16.8. The expected spot has a size of 11.9 μm × 1.2 μm (X × Y), naturally presenting the same elongation as the source. On the other hand, a secondary source can be formed at 12.1 m downstream of the undulator by using a horizontally tunable slit, as shown in Figs. 1(b) and 1(c), which can be used for obtaining a smaller horizontal spot size. However, by using circular FZPs the distance between both foci would be of the order of 72 mm, thereby preventing either isotropic resolution in a scanning-probe experiment, or at the cost of a lower resolution by working in the circle of least confusion. In order to account for the different source locations in both dimensions, we designed elliptical FZPs which, by construction, have a different focal length along the main axes, see Fig. 1(c). Elliptical FZPs were successfully produced in the past for correcting astigmatism originating from upstream optics [22]. Without loss of generality, as the focal length f_1, the aperture A and the outermost zone width Δr of a FZP satisfy $A\Delta r = \lambda f_0$, where λ is the X-ray wavelength, one can scale the focal length from f_0 to $f_1 = \eta f_0$ by multiplying both A and Δr with $\sqrt{\eta}$. This solution geometrically corresponds to a global scaling in 1D of all zone widths that constitute the FZP. Using elliptical FZPs thus makes it possible to cancel out the on-axis astigmatism of the incoming beam, caused by the strategy proposed here for obtaining a round microbeam. Importantly, as the slit producing the secondary source is tunable, our setup allows for changes of the horizontal beam spot without affecting the vertical one, with both beam size and intensity being proportional to the slit opening. Demagnification factors of 10.4 and 16.8 are obtained in X and Y, respectively. With this strategy, the spot has an expected size of 1.9 μm × 1.2 μm (X × Y) when the slit is closed to 20 μm.

We note that due to the location of the undulator source in the electron storage ring of the synchrotron it is not possible to install a slit close to the source, which would produce an isotropic source size at $Z_f -33.8$ m from the sample. A rectangular slit could be used to define an isotropic source at $Z_f -21.7$ m, however this would require reducing the aperture to achieve the same focus dimensions at the sample position, which would decrease the intensity in the focused beam.

The FZPs were patterned by electron-beam lithography (EBL, Vistec EBPG 5000plus, Raith GmbH). Gold (Au) or nickel (Ni) was electroplated into the polymethyl methacrylate (PMMA) molds obtained after development [23, 24]. The material of each FZP was chosen for minimizing X-ray absorption at the intended energy, using Ni for energies below the Ni K-edge at 8.33 keV and Au for higher energies. A set of FZPs with identical focal lengths were designed and fabricated for photon energies corresponding to odd-numbered undulator harmonics, providing highest flux, i.e. 6.2, 8.7, 11.2, and 13.6 keV, and for 12.4 keV corresponding to the wavelength of 1 Å. Depending on the energy, either the aperture was limited to 900.0 μm, which is the maximum allowed aperture by the beamline transport tubes, or the outermost zone width down to 250 nm so that the required height for the metal structures could be achieved, due to limitation in the reachable aspect ratio in the nanofabrication process. Both a circular and an elliptical FZP were fabricated for all energies. The metal thickness was adjusted to closely provide an optimal phase shift of π radians onto the incoming beam at each energy. The circular FZPs parameters are summarized in Table 1, see also Figs. 2(a)–2(c).

Table 1. Circular FZPs parameters. The focal length for all energies is $f_0 = 1793$ mm.

Energy	6.2 keV	8.7 keV	11.2 keV	12.4 keV	13.6 keV
Aperture A	900.0 µm	900.0 µm	794.1 µm	717.3 µm	654.0 µm
Outermost zone width Δr	398.5 nm	284.0 nm	250.0 nm	250.0 nm	250.0 nm
Height h	2.35 µm	1.70 µm	2.25 µm	2.25 µm	2.50 µm
Material	Ni	Au	Au	Au	Au

We designed the elliptical optics by horizontally scaling the electron-beam writer patterns of the circular FZPs by a factor of 0.9833. To do so, different sub-field resolutions of the electron-beam writer were set in X and Y, and the central coordinates of the main fields were adjusted to ensure continuity at stitching boundaries. As an illustration with the elliptical FZP designed at 11.2 keV, the aperture resulting along the horizontal axis is 780.8 µm, compared to 794.1 µm along the vertical one. The precision required is easily provided by our EBL tool, which has placement accuracy lying in the nanometer range. The flexibility of the EBL technique thus makes it possible to obtain elliptical optics at no additional cost in the fabrication process.
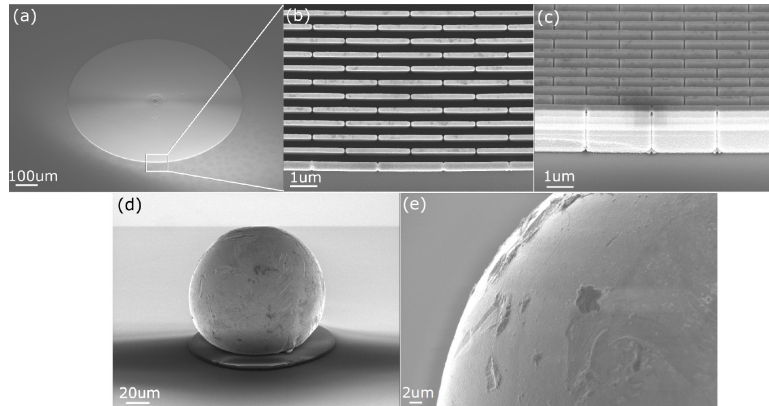

Fig. 2. Scanning electron microscope micrographs of X-ray optics components. (a) Overview of the circular FZP designed for 11.2-keV radiation with an aperture of 794.1 µm. Outermost zones with linewidth of 250 nm and height of 2.25 µm are shown in (b) top view and (c) 45° tilted view. (d) 70° tilted view of a Au80Sn20 central stop, with diameter in the range of 100 µm, and (e) close-up view.

Central stops were made of a eutectic alloy with composition Au80Sn20 in weight ratio. The advantage of using such a material is its relatively high density (*i.e.* 14.7 g/cm^3), which makes it a good absorber for multi-keV X-rays while having a rather low melting temperature of ~280°C. The raw material comes in the form of a 100-µm diameter wire (IPT-Albrecht GmbH). Pieces of such a Au80Sn20 wire were heated up to 300°C using a soldering iron, then cut with dimensions in the range of a few hundreds of microns, and placed in contact of a soldering fluid. The material formed spheres with diameters in the range of a few tens to several hundreds of microns. After cooling down and rinsing in water and isopropyl alcohol, a sphere with suitable diameter for our application was centered on top of a 2-µm thick silicon membrane (Norcada Inc.) using a micromanipulator and then held by placing a similar membrane upside-down. The two membrane frames were glued face to face using low-temperature Crystalbond^{TM} wax heated at 120°C for one minute. In Figs. 2(d) and 2(e), scanning electron microscope

micrographs of a Au80Sn20 central stop with diameter of about 100 μm are shown. In the following experiments, the central stop used had a diameter of about 160 μm.

3. Beam characterization

We report here the characterization of both the circular FZP in absence of a secondary source and of the elliptical FZP with the slit set to a horizontal opening of 20 μm, at photon energy of 11.2 keV (wavelength of 0.111 nm). We do not expect significant differences at other photon energies.

3.1 Knife-edge scans

We first performed knife-edge measurements using 100-μm diameter steel crossed wires, in order to determine the location of the foci along Z. The transmitted intensity was measured using a photodiode, and both wires were successively scanned through the beam using a piezoelectric nanopositioning stage with a step of 500 nm. This was repeated at different locations along Z. The beam spot size was estimated with the absolute value of the derivative of the knife-edge signal with respect to the spatial coordinate. Gaussian fits were used for determining the full-width half maximum (FWHM), assuming that the source intensity can be well approximated by a two-dimensional Gaussian distribution [25].
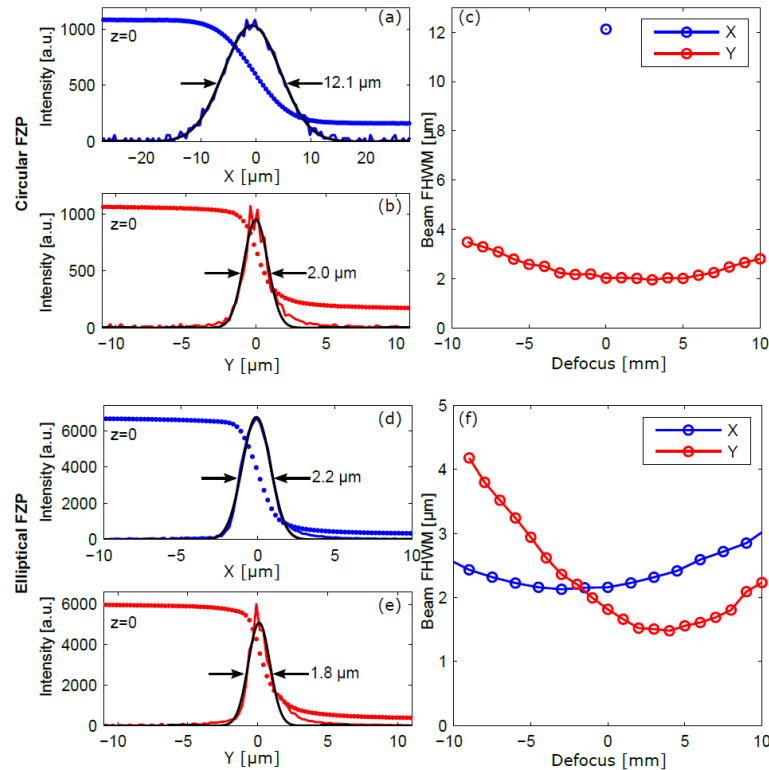

Fig. 3. Knife-edge measurements. (a-c) Using the circular FZP and no secondary source. (d-f) Using the elliptical FZP and a secondary source of 20 μm. (a-b) and (d-e) Intensity profiles along both axes for knife-edge scans (dots) and absolute derivatives (solid colored line). Black solid lines are Gaussian fits, the FWHM of which are given. (c) and (f) show the beam FWHM versus defocus.

Using the circular FZP with no secondary source, a focused size of 12.1 μm × 2.0 μm (X × Y) was measured in the focal plane, see Figs. 3(a) and 3(b), to be compared to the expected values of 11.9 μm × 1.2 μm (X × Y). Using the elliptical FZP with the horizontal slit defining a secondary source of 20 μm a focused size of 2.2 μm × 1.8 μm (X × Y) was measured in the same plane in Z, see Figs. 3(d) and 3(e), to be compared to

the expected values of 1.9 μm × 1.2 μm (X × Y). Both measurements result in beam sizes larger than the calculation. This may be an indication that the finite sharpness of the used wires has an influence on the knife-edge measurement, leading to the beam size being overestimated. The values given are therefore upper limits of the actual size. Finally, the beam caustics in the case of astigmatism correction are shown in Fig. 3(f) and demonstrate good positioning of the horizontal and vertical foci along Z within the depths of focus, which are of 12.7 mm and 5.4 mm, respectively, validating the strategy proposed in this work. The distance of about 7 mm between both foci could be due to uncertainties in the slit position along Z, or in the actual position of the source within the undulator. Similarly, optical aberrations originating from upstream optics could contribute to the error. In particular, either the monochromator or the high-harmonic rejection mirror can be the source of wavefront aberrations [25] that could possibly affect the beam divergence differently in the horizontal and vertical dimensions.

3.2 Scanning transmission X-ray microscopy measurements on test objects

For an accurate characterization of the achieved resolution we performed scanning transmission X-ray microscopy (STXM) measurements on test objects using a photodiode. Two test objects were considered, firstly chirped gratings (*i.e.* presenting a spatial variation in the grating period perpendicular to the grating lines) with largest pitch of 40 μm down to 500 nm, and secondly Siemens stars with inner spoke linewidth of 500 nm. The test objects were made by gold electroplating with thickness up to 2.1 μm into a PMMA mold fabricated using EBL [24]. STXM scans were performed for both objects, in one dimension with a step of 500 nm for chirped gratings, and in two dimensions with steps of 2 μm for Siemens stars, using stages with positioning precision better than 1 μm.

When scanning chirped gratings, a variation of the transmitted X-ray beam between a maximal value S_{max} and a minimal value S_{min} is observed, due to the absorption of the periodic gold structures. The visibility V defined as $V = (S_{max} - S_{min})/(S_{max} + S_{min})$ is determined at different spatial frequencies and, when normalized to the reference visibility for infinitely large grating period, V_0 = 15.3%, leads to the modulation transfer function (MTF) of the optics, see Fig. 4. V_0 was obtained by determining the transmission of a gold structure with height of 2.1 μm and estimated density of 17 g/cm^3 for the electroplated metal.

The two main cases of interest are using the circular FZP with no secondary source, see Fig. 4(b), and the elliptical FZP with the horizontal slit defining a secondary source of 20 μm, shown in Fig. 4(e). The vertical MTF (see red triangles) remains closely similar between the two cases and spatial frequencies of more than 250 mm^{-1} are revealed – corresponding to 2-μm features. On the other hand, the visibility along the horizontal direction (see blue dots) undergoes a dramatic improvement – from cutoff spatial frequency in the range of 50 mm^{-1} in Fig. 4(b) to more than 250 mm^{-1} as well in Fig. 4(e). The fact that in Fig. 4(e) the visibility has not decreased to zero at 250 mm^{-1} signifies that in this case the accuracy was limited by the translation stages which did not permit precise visibility measurement at higher spatial frequencies. Observing the STXM Siemens star scans, shown in the second column in Fig. 4, when using a secondary source of 20 μm and the elliptical FZP, see Fig. 4(e), in which features between the 1-μm and the 2-μm interruptions in the star pattern are revealed, exemplify that a resolution better than 2 μm is achieved.
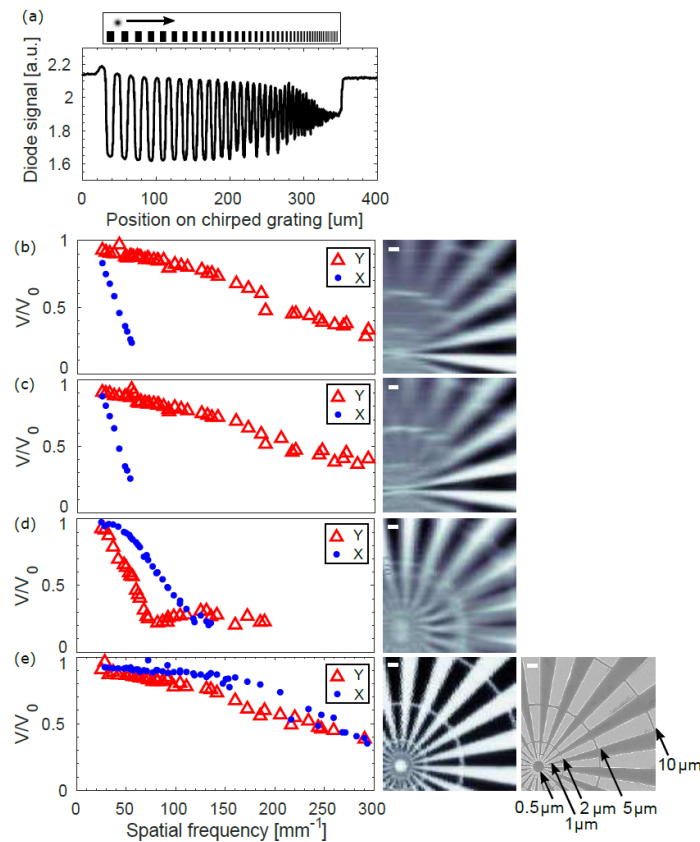
Fig. 4. Resolution measurements. (a) Example of a transmission scan of an X-ray beam across gold chirped gratings (see inset above). This leads to the modulation transfer functions in case of (b) the circular FZP with no secondary source, (c) the circular FZP used with a secondary source of 20 μm at same focal plane and (d) at the circle of least confusion, and (e) the elliptical FZP used with same secondary source. The visibility V is normalized to V_0 (see text). Visibilities V below 3% are discarded due to experimental uncertainties. Correspondingly, STXM scans of Siemens stars are shown on the right, with a scanning electron microscope micrograph (bottom right) indicating the local linewidth in the Siemens star. The scale bar indicates 5 μm in all images.

For completeness two additional situations were considered. In Fig. 4(c) the visibility obtained when using the circular FZP and a secondary source of 20 μm is shown – while in Fig. 4(d) the same arrangement is used, but with the test object placed in the circle of least confusion, corresponding to Fig. 1(b). Placing the test object in the circle of least confusion was achieved by temporarily setting the photon energy to 11.01 keV and exploiting the chromaticity of the FZP. These cases are instructive in that they reveal the best resolution obtainable with a circular FZP, providing a fair basis to compare to the performance achieved with our device. It can first be concluded that creating a secondary source while using the circular FZP does not improve the resolution in X, as shown in Fig. 4(c). Second, the horizontal spatial frequency cutoff is modestly improved to about 100 mm^{-1} when working in the circle of least confusion shown in Fig. 4(d), however at the cost of an important decrease in the vertical resolution. Furthermore, in this case, contrast inversion due to strong astigmatism can be observed above spatial frequencies of about 75 mm^{-1}, manifesting itself as a local decrease of the vertical MTF towards zero observed at about 75 mm^{-1}. This is visible in the Siemens star image, see Fig. 4(d), in which the horizontal spokes, corresponding to the vertical resolution, have inverted contrast between above and below a linewidth of approximately 6 μm.

3.3 Ptychographic reconstruction

To further characterize the lens performance, we performed ptychography measurements at 11.2 keV. Over the last years, ptychography has been proven to be a robust tool for high-resolution X-ray imaging [26–29] with the ability to simultaneously reconstruct at the sample position the complex-valued object transmissivity function and the illumination function, often referred to as object and probe, respectively. This is achieved by scanning a coherently illuminated specimen along two axes perpendicular to the beam propagation direction and collecting far-field diffraction patterns for each position. A central tenet of a ptychographic scan is that adjacent illuminated regions are overlapping, allowing a robust iterative solution of the phase-retrieval problem. The reconstructed probe can be used for further investigation of the beam at any distance from the object, including at the entrance pupil plane of the lens [30–33] and even to apply subsequent corrections to the optical elements [34]. As a test pattern, we used a hydrogen silsesquioxane (HSQ) Siemens star with a structure height of 700 nm fabricated using 100-keV EBL. The sample was coated with a layer of iridium (Ir) with thickness of 10 nm using atomic layer deposition. 2D ptychography measurements of the same test object have been published elsewhere [26]. We performed a scan consisting of 819 positions following a Fermat spiral [35] across a field of view of 10 μm × 10 μm with an average step size of 0.35 μm. Using the elliptical FZP, diffraction patterns with an exposure time of 0.2 s were recorded using an Eiger detector [36] with a pixel pitch of 75 μm at a distance of 7.21 m from the sample. The transverse coherence length at the FZP was significantly smaller than the lens diameter, which made ptychography measurements more stringent and reconstructions more challenging. To improve the transverse coherence of the beam, the horizontal slit aperture, at a distance of 12.1 m downstream of the source, was closed to 5 μm, resulting in a transverse coherence length of 391 μm × 155 μm (X × Y) at the FZP position, which is nevertheless smaller than the FZP diameter of 794.1 μm. To account for the partially coherent illumination of the specimen, we used mixed-states reconstruction algorithms, representing the illumination, in this case, via 6 mutually incoherent modes [37]. As the illumination starting guess, a set of 6 simulated modes was defined. We used 5000 iterations of difference map followed by 1000 iterations of maximum likelihood refinement and a probe support radius of 80% of the computational window width.

To further aid with convergence, the probe support was reduced to 40% before subsequently performing another 2000 iterations of difference map and 1000 iterations of maximum likelihood refinement. Key features of the Siemens star object are easily recognized in the object reconstruction, shown in Fig. 5(e), in particular the different phase shifts of the spokes with respect to the substrate and the dark lines surrounding the object which correspond to the thin Ir layer. A comparison can be made with a similar test sample shown in Ref. 26, where a smaller FZP was illuminated coherently. Upon comparison, it can be observed that the reconstruction in Fig. 5(e) shows some low-frequency artifacts and faint halos around the structures. This could arise from the increased difficulty in reconstructing the data set due to the low degree of coherence which entails some loss of information. Alternatively, we have also observed radiation damage on these structures upon repeated scanning, in this case the sample was illuminated with a significantly higher photon flux density compared to Ref. 26, and it could be that the halos arise as a compensation mechanism of the algorithm to a changing sample. The appearance of expected features in the reconstruction, along with the good agreement of the illumination with knife-edge scans taken at different propagation distances give us confidence in the reconstruction.
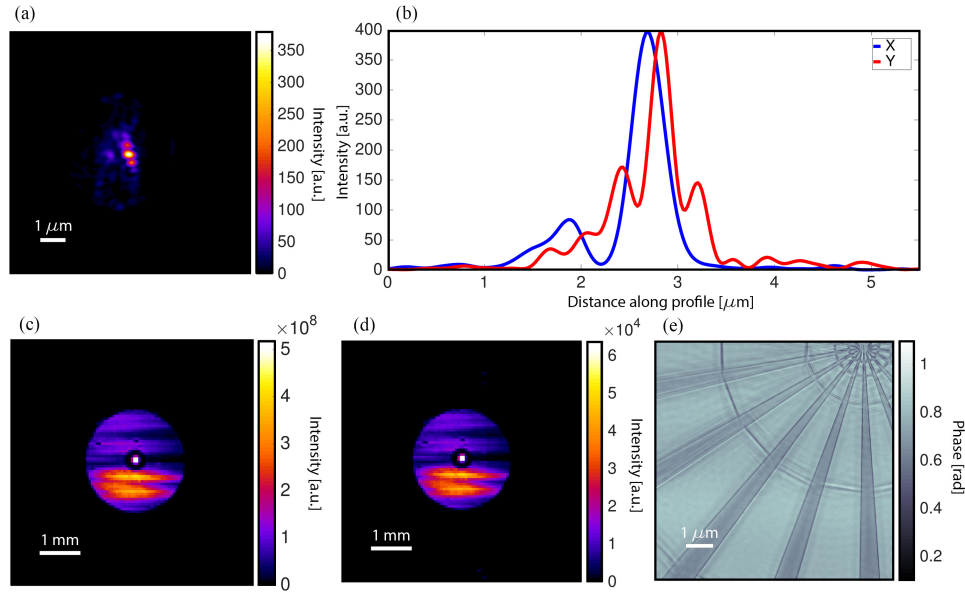
Fig. 5. Beam characterization by X-ray ptychography, with horizontal secondary source of 5 μm. (a) Intensity of reconstructed focused beam at the focal plane. (b) Line profiles across the focus intensity in (a) along the vertical (red) and horizontal (blue) directions. The (c) reconstructed beam propagated to the detector plane can be compared to a (d) diffraction pattern of a single measurement. (e) Phase of the reconstructed object transmissivity.

The beam intensity at any plane can be calculated by individually propagating each reconstructed mode and adding their intensities. The beam profile at the focus is shown in Fig. 5(a) of which the horizontal and vertical profiles are plotted in Fig. 5(b). In the horizontal direction, the beam FWHM is 0.4 μm, to be compared to the expected demagnified image of the horizontal aperture slit of 0.48 μm. The beam vertical FWHM also matches well the 1.2-μm image of the demagnified source. However, in contrast to a diffraction-limited beam, the reconstruction has increased amplitude of sidelobes and asymmetric structure. As mentioned earlier, these structures can be caused by optical aberrations introduced by the upstream optics of the beamline. The presence of phase aberrations upstream of the lens can be inferred from the non-uniform illumination at the plane of the lens. For instance, the horizontal stripes in the intensity pattern recorded at the detector, Fig. 5(d), appear on the detector almost identically as they occur at the entrance pupil of the lens and possibly originate from optical aberrations introduced further upstream. The asymmetric structure of the beam in the vertical direction is consistent with that caused by a third-order polynomial aberration, as was observed in [32], which is likely caused by upstream beamline optics.

3.4 Flux and efficiency measurements

The integrated microfocus efficiency, defined as the flux diffracted into the first order normalized to the incoming flux with no zone plate and no central stop, was measured at 11.2 keV to be 23.1% for the circular FZP and 22.5% for the elliptical FZP. The total incoming flux was further determined based on measurements on a calibrated glassy carbon sample with thickness of 1 mm [38]. In the setup with the circular FZP and no secondary source, corresponding to Fig. 1(a), the estimated incident photon flux on the sample is 1.2×10^{11} photons/s and the estimated photon flux density is 4.9×10^{9} photons/s/μm^2. In the setup with the elliptical FZP and secondary source of 20 μm, corresponding to Fig. 1(c), the estimated incident photon flux on the sample is 1.2×10^{10} photons/s and the estimated photon flux density is 3×10^{9} photons/s/μm^2.

4. Microfocus scanning SAXS measurements

As an example of measurement opportunities offered by this microfocus setup, scanning SAXS measurements were performed at 11.2 keV on 20-μm slices of human trabecular bone using the newly developed microfocusing. Bone is heterogeneous at all hierarchical levels of organization and, in that sense, represents an excellent benchmark for the scanning SAXS technique [9,39–42]. Vertebrae were obtained from the Department of Anatomy, Histology, and Embryology at the Innsbruck Medical University, Innsbruck, Austria, with the written consent of the donors according to Austrian law. All following procedures were performed in accordance with Swiss law, the Guideline on Bio-Banking of the Swiss Academy of the Medical Science (2006) and the Swiss ordinance 814.912 (2012) on the contained use of organisms.

Scattering patterns were acquired with a Pilatus 2M detector [43]. A 7.15-m long vacuum flight tube was installed between the sample and the detector to limit the parasitic scattering in air. The field of view in the scan was 402 μm × 210 μm (X × Y) with steps of 2 μm in both directions. Data were acquired during a continuous movement of the sample along the horizontal direction following a snake pattern in which the movement direction was changed after moving the sample in the vertical direction to scan the next line. In this way the measurement overhead between acquisitions of individual lines was minimized. Absorption and orientation images obtained with the circular FZP and no secondary source are shown in Figs. 6(a) and 6(b). In this case the spot size on the sample was 12.1 μm × 2.0 μm (X × Y). Orientation images are obtained as described in Ref [44]. and represent the orientation of the SAXS patterns recorded at each point on the image, which is related to the orientation of the nanostructures in the bone tissue [41,42]. Similar images obtained using the elliptical FZP and a secondary source of 20 μm are shown in Figs. 6(c) and 6(d), with a spot size of 2.2 μm × 1.8 μm (X × Y). When using the circular FZP and no secondary source, the acquisition time was 30 ms with 5 ms readout time, see Figs. 6(a) and 6(b). To account for the lower photon flux implied by using the secondary source of 20 μm, the acquisition time was then increased to 80 ms with the same readout time, see Figs. 6(c) and 6(d). Assuming a Poisson noise model, this theoretically results in a loss of signal to noise ratio of a factor of 1.9 that is, however, far from presenting any limitation in signal quality, as demonstrated in Fig. 6(c). In Fig. 6(e) scattering patterns are shown for the case with finest resolution of Fig. 6(d), from selected points with different local orientations, as well as the integrated data over 8 angular sectors distributed from 0 to 180 degrees, note that the sectors average the signal with the centrosymmetric counterpart. When comparing the two data sets in Figs. 6(a) and 6(b), and Figs. 6(c) and 6(d), one observes that more structural changes over the characteristic length scale explored with the microfocus beam are revealed with the finer beam. For instance, small inclusions showing different orientations now appear in many areas, which are otherwise dominated by the averaged orientation when measured with a beam of 20 μm [44].
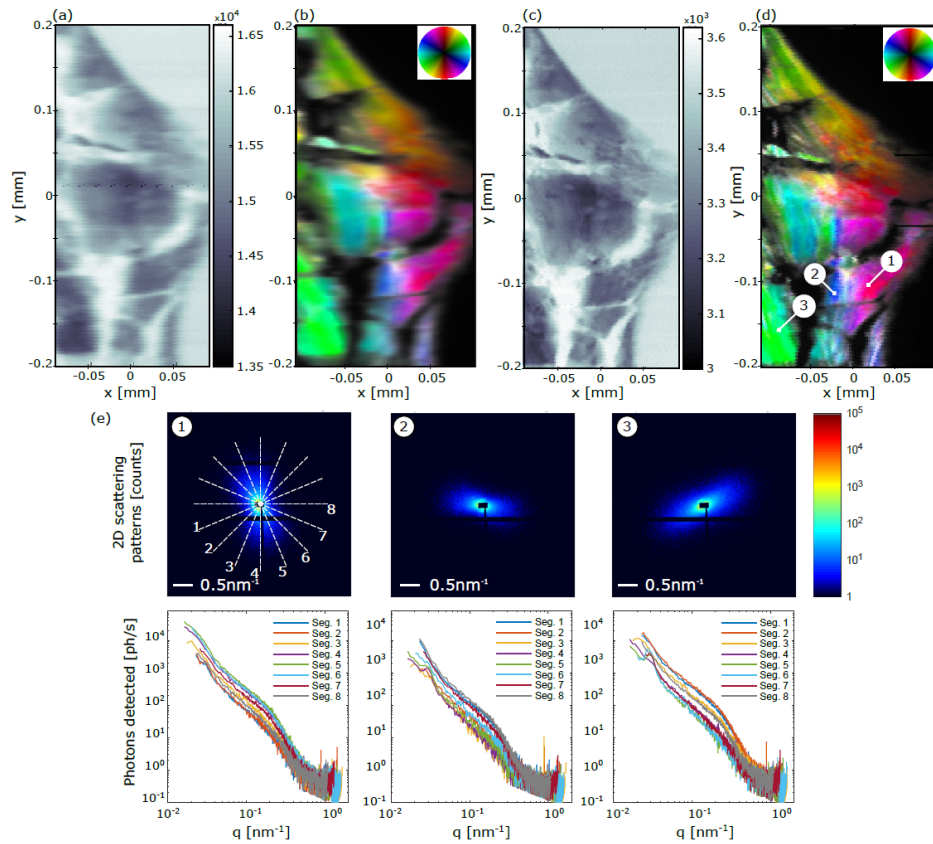
Fig. 6. Scanning SAXS measurements at 11.2 keV on thin slice of human trabecular bone. (a) and (b) were acquired using the circular FZP producing a beam with size of 12.1 μm × 2.0 μm (X × Y), whereas (c) and (d) were acquired using the elliptical FZP and a secondary source of 20 μm, producing a beam of 2.2 μm × 1.8 μm (X × Y). (a) and (c) are intensity absorption images (see color bar in fixed arbitrary units); (b) and (d) are orientation images obtained after azimuthal integration in the range 109.57 nm to 164.36 nm in the real space, and post-treatment of the far-field signal [45]. The isotropic scattering intensity is represented by image intensity, the degree of orientation by the color saturation and the main scattering orientation by the hue as shown in the color wheel. Panel (e) shows single scattering patterns as observed on the detector at 3 different points as numbered on panel (d), to emphasize the local structure orientation. Below each scattering pattern we show the signal integrated over 8 angular sectors that are sketched in the scattering pattern numbered 1, versus the scattering vector **q**.

5. Discussion and conclusion

In this work, a strategy to compensate for the elongated shape of X-ray beams generated by synchrotron sources for performing microprobe experiments with isotropic resolution has been proposed, implemented and commissioned at the cSAXS beamline at the Swiss Light Source. In order to maximize the flux at the focus the FZP operates with performance limited by geometrical source demagnification and wavefront aberrations introduced by beamline optics. Using a combination of a secondary horizontal source, defined by a slit, and elliptical FZPs we obtained a round beam allowing for microfocus experiments at multi-keV photon energy with resolution better than 2 μm and a photon flux of the order of 1.2×10^{10} photons/s. We have verified the resolution achieved by standard approaches and the beam propagation has been further analyzed using ptychography. Our imaging system offers a large flexibility in horizontal beam size since the secondary source size can be arbitrarily chosen. For example, a horizontal resolution set in the range of 5 μm and a correspondingly higher photon flux by a factor of 2.5 can be advantageous for certain microprobe experiments. In such a case, to keep the

resolution isotropic, continuous scanning in the vertical direction could be used. One could then choose an appropriate speed of the vertical stage such that acquisitions of a certain integration time would average the scattering signal over a vertical length equal to the desired pixel size.

Several advantages of using diffractive FZPs in context of microprobe experiments can be pointed out. Since the outermost zone width of the required optics lies in the micrometer range, the optimum height for binary structures to reach local phase shift of π for optimal efficiency at multi-keV photon energies can usually be achieved in a single-step lithographic process, as demonstrated here. Interestingly, the coherence length determined by the source does not limit the aperture since diffraction-limited performances are not sought, leading here to apertures as high as 0.9 mm. A microfocus module based on diffractive elements finally offers the option of placing the module in and out of the beam depending on the needs by a simple translation, since no modification of the optical axis is needed and no angular alignment is required.

These experiments will be extended to SAXS tensor tomography [41], which will enable the measurement of nanostructure orientations spatially resolved in 3D with a resolution better than 2 μm. More generally, our work may foster the use of other multi-keV X-ray microprobe techniques for which an equal resolution along both dimensions in the micrometer range is crucial, while maintaining a photon flux delivered to the interaction point as high as possible.

Acknowledgments